

# Automatic source localization and spectra generation from deconvolved beamforming maps

A. Goudarzi\* and C. Spehr\*

*German Aerospace Center (DLR), Göttingen, Germany*

S. Herbold†

*Institute AIFB, Karlsruhe Institute of Technology (KIT), Karlsruhe, Germany*

We present two methods for the automated detection of aeroacoustic source positions in deconvolved beamforming maps and the extraction of their corresponding spectra. We evaluate these methods on two scaled airframe half-model wind-tunnel measurements. The first relies on the spatial normal distribution of aeroacoustic broadband sources in CLEAN-SC maps. The second uses hierarchical clustering methods. Both methods predict a spatial probability estimation based on which aeroacoustic spectra are generated.

## Nomenclature

### *Variables*

$\alpha$	Angle of attack in deg
$f$	Frequency in Hz
$f_s$	Sample frequency in Hz
$M$	Mach number
$s$	Source-part
$\sigma$	Standard deviation
St	Strouhal number
$T$	Temperature in Kelvin

### *Abbreviations*

CLEAN-SC	CLEAN based on Source Coherence
CSM	Cross-Spectral density Matrix
DAMAS	Deconvolution Approach for the Mapping of Acoustic Sources
DR	Diagonal Removal
HDBSCAN	Hierarchical Density-Based Spatial Clustering of Applications with Noise
PCA	Principal Component Analysis
PDF	Probability Density Function
PSD	Power Spectrum Density in dB (ref. $p_0 = 4 \times 10^{-10} \text{ Pa}^2$ )
PSF	Point Spread Function
ROI	Region Of Interest
SIND	Source Identification based on spatial Normal Distribution
SIHC	Source Identification based on Hierarchical Clustering

---

\*armin.goudarzi@dlr.de, carsten.spehr@dlr.de

†herbold@cs.uni-goettingen.de

### Subscript

$i$	Variable index
$\langle \dots \rangle_i$	Mean over $i$

## I. Introduction

Multiple noise-generating phenomena and mechanisms exist in aeroacoustics.<sup>7,11</sup> Expert domain knowledge and a detailed study of measurements is necessary to identify these phenomena in measurements. For localization and estimation of the sound power of aeroacoustic sources, beamforming is a reliable method.<sup>10</sup> Beamforming results in high dimensional maps ( $\text{PSD}(\vec{x}, f, M, \dots)$ ) that are difficult and time consuming to analyze manually. Therefore, resulting beamforming maps are usually integrated over space and frequency areas to obtain low dimensional data such as spectra<sup>9</sup> which can be interpreted by human experts. In this paper, we present two approaches to automatically identify stationary, aeroacoustic sources and obtain their spectra from deconvolved beamforming maps. We use the scaled air-frame models of a Dornier 728<sup>1</sup> and an Airbus A320<sup>2</sup> to derive these methods, discuss their usefulness and specify a proof-of-concept implementation.

## II. Datasets

The data used in the present paper consists of beamforming measurements of two closed-section wind-tunnel models: one is of a Do728<sup>1</sup> and one is of an A320.<sup>2</sup> For the Do728 dataset, values of  $\alpha_i = 1^\circ, 3^\circ, 5^\circ, 6^\circ, 7^\circ, 8^\circ, 9^\circ, 10^\circ$  are chosen for angle of attack and  $M_i = 0.125, 0.150, 0.175, 0.200, 0.225, 0.250$  for Mach number. The mean Reynolds number is  $\langle \text{Re} \rangle_M = 1.4 \times 10^6$  based on the mean aerodynamic cord length  $D_0 = 0.353$  m and ambient temperature of  $T = 300$  K. The array consists of 144 microphones at an aperture of  $1.756 \text{ m} \times 1.3 \text{ m}$  and a sample frequency of  $f_S = 120$  kHz. The A320 set contains  $\alpha_i = 3^\circ, 7^\circ, 7.15^\circ, 9^\circ$ ,  $M_i = 0.175, 0.200, 0.225$  at a mean Reynolds number of  $\langle \text{Re} \rangle_M = 1.4 \times 10^6$  based on  $D_0 = 0.308$  m,  $T = 300$  K. The array consisted of 96 microphones at an aperture of  $1.06 \text{ m} \times 0.5704 \text{ m}$  and  $f_S = 150$  kHz. Thus, we use 48 measurements for the Do728 and 12 measurements for the A320 dataset. We calculate Cross-Spectral density Matrices (CSM) using Welch's method with a block size of 1024 samples for the Do728 and 512 samples for the A320 with 50 % overlap. The beamforming is performed using conventional beamforming and CLEAN-SC deconvolution with a focus point resolution of  $\Delta x_1 = \Delta x_2 = 5 \times 10^{-3}$  m.

## III. Source identification

A general problem concerning beamforming is that at low wavelengths the localization of acoustic sources becomes more difficult. Furthermore, acoustic artifacts may occur due to the sparse spatial distribution of the microphone array. These artifacts result from background noise, the array's Point Spread Function (PSF), and aliasing or insufficient Welch estimations.<sup>10</sup> In this part of the paper, we discuss two ideas on how to identify sources from beamforming maps contaminated with noise and obtain their spectrum. The ideas are based on sparse beamforming maps which can be achieved by inverse beamforming methods or conventional beamforming<sup>10</sup> in combination with what is known in the aeroacoustic beamforming community as "deconvolution", such as CLEAN-SC<sup>13</sup> or DAMAS.<sup>3</sup> For this paper, we choose conventional beamforming with diagonal removal<sup>10</sup> in combination with CLEAN-SC over DAMAS, because of the huge number of computed beamforming maps and the high spatial resolution of the maps. CLEAN-SC assumes point-like sources and then subtracts coherent portions of the dirty beamforming map.<sup>13</sup> This removes the PSF but will also result in a single  $\text{PSD}(\vec{x}_0, f_0)$  representation of spatially expanded sources. We make this an advantage as this results in extremely sparse representations of the source map. For the terminology, we call every  $\text{PSD}(\vec{x}_0, f_0)$  reconstructed by CLEAN-SC from the dirty map a source-part  $s$ . Thus, the result of CLEAN-SC is a list of source-part vectors  $s_i = [\vec{x}_i, f_i, M_i, \text{PSD}_i]$ . Figure 1 displays the source-parts of the CLEAN-SC result on a 2D-focus grid of the A320. On the z-axis, the frequency is displayed, the color represents the normalized PSD. We can identify multiple vertical pillars of source-parts  $s$  that spatially integrated represent a source spectrum  $\text{PSD}(f)$ . However, we also observe pillars that suddenly split with increasing frequency (e.g., at the flap side edge) or pillars with higher density embedded in blobs with lower density (e.g., the slat track at the inner slat). Up to now, large Regions Of Interest (ROI) were defined as integration areas

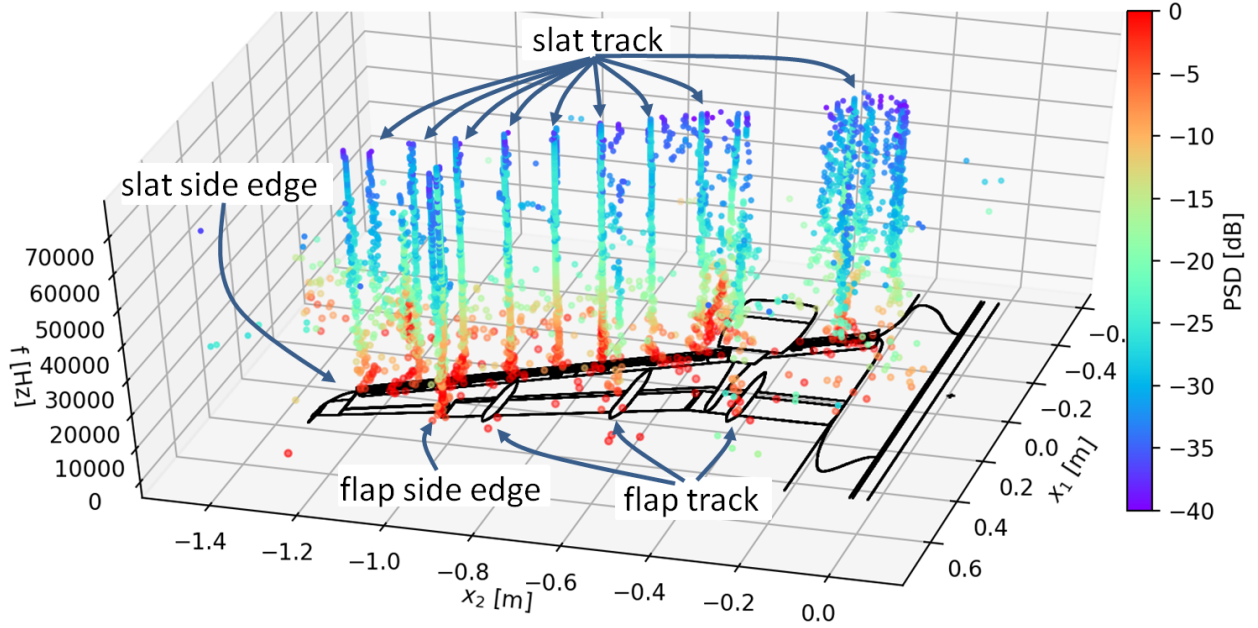


Figure 1: A320, CLEAN-SC result on 2D-plane using conventional beamforming, the z-axis displays the frequency. The color represents the normalized PSD in decibel.  $\Delta x_1 = \Delta x_2 = 5 \times 10^{-3}$  m, Welch blocksize = 256,  $M = 0.2$ ,  $\alpha = 3^\circ$ .

to obtain spectra<sup>12</sup> such as the whole slat and flap region. This partly contradicts the beamforming idea, as we often do not know where sources are located and whether all sources within the integration region are of the same source type. In the following part, we introduce two methods on how to estimate the existence and positions of individual sources and how to correctly assign them the corresponding source-parts.

### A. Source Identification based on spatial Normal Distributions (SIND)

Figure 2 *a*) shows the normalized Overall Sound Pressure Level (OASPL) at all locations  $\vec{x}$  for the A320. The OASPL is the integration of the source-parts level over frequency. We observe that sources cannot be easily distinguished based on the OASPL because the sound carries most energy at long wavelengths at which beamforming is not able to localize sources well due to the array resolution (see also Figure 1). However, ignoring the PSD and simply counting how often a source-part  $s$  was reconstructed by CLEAN-SC at every location  $\vec{x}$  provides a better grasp on individual source distributions, which can be seen in the logarithmic histogram in Figure 2 *b*). We see mostly distinguishable blobs with maxima in their center that probably represent sources. In this case, the blob's positions correlate with the location of the slat tracks, the slat side edge, and the flap side edge. While the blobs in the log-histogram resemble normal distributions, statistical tests such as the Shapiro-Wilk or Anderson-Darling test would still not determine that data as normal. The reason for this is the discrete spatial sampling as well as the large population of source-parts. Instead, we use a soft normal distribution test to verify the normality assumption. First, we fit a normal distribution to the log-distribution of the appearance of source-parts by minimizing the difference between the source-part position histogram and the estimated Probability Density Function (PDF). Then, we compare the estimated distribution with the observed data. The normal distribution in 2D is calculated with eq. 1. For practical applications, we recommend optimizing for  $A, \sigma_{x_i}, \theta, x_{i,0}$  by using a bounded optimization method. The histograms maximum determines the starting values for  $A, x_{i,0}$ , the bounds  $A \pm \varepsilon_A, \vec{x} \pm \varepsilon_{\vec{x}}$  prevent the optimizer from wandering off to a completely different blob.

$$f(x_1, x_2) = A \exp \left( - \left( a(x_1 - x_{1,0})^2 + 2b(x_1 - x_{1,0})(x_2 - x_{2,0}) + c(x_2 - x_{2,0})^2 \right) \right) \quad (1)$$

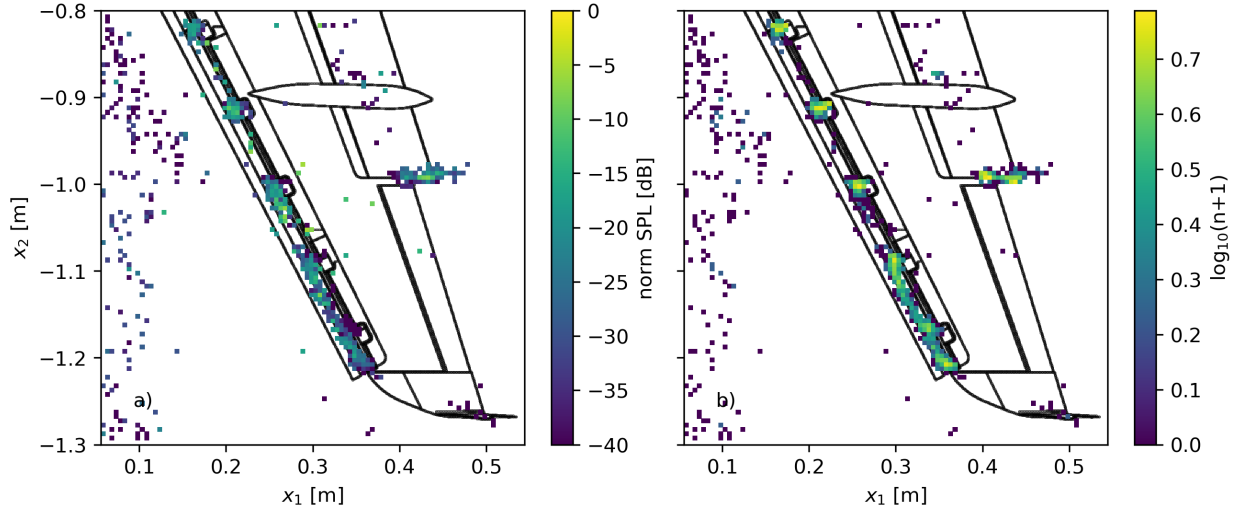


Figure 2: A320, section of the deconvolved source map at  $M = 0.175, \alpha = 3^\circ$ . *a)* shows the normalized OASPL, *b)* shows a log-histogram of the source-parts  $s$  per focus point  $\vec{x}$ . Welch blocksize = 512, focus point resolution  $\Delta x_1 = \Delta x_2 = 5 \times 10^{-3}$  m.

$$a = \frac{\cos^2 \theta}{2\sigma_{x_1}^2} + \frac{\sin^2 \theta}{2\sigma_{x_2}^2} \quad (2)$$

$$b = -\frac{\sin 2\theta}{4\sigma_{x_1}^2} + \frac{\sin 2\theta}{4\sigma_{x_2}^2} \quad (3)$$

$$c = \frac{\sin^2 \theta}{2\sigma_{x_1}^2} + \frac{\cos^2 \theta}{2\sigma_{x_2}^2} \quad (4)$$

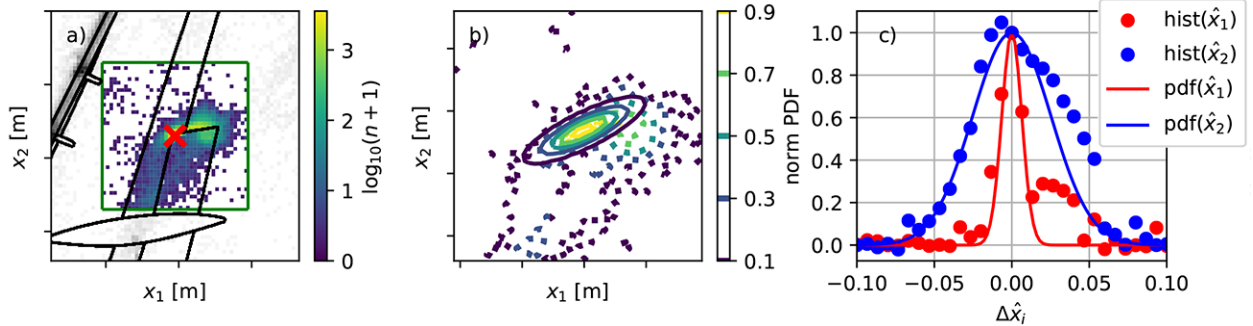


Figure 3: Do728, flap side edge. *a)* shows the log-histogram of the source-parts over all  $M_i, \alpha_i$  and  $f_i$  and its peak (red x). *b)* shows the isocontour lines of the by  $A$  normalized distribution (dotted lines) and its fitted PDF (full lines). *c)* shows the normalized distribution and PDF on its principal axis  $\hat{x}_1$  and  $\hat{x}_2$ .

Figure 3 *a)* shows the log-distribution of the source-parts for the Do728 flap side edge. We can determine a major blob within the marked green area. In *b)* isocontour lines of the actual distribution (dotted) and the fitted normal distribution are shown. We introduce two principal axes  $\hat{x}_1$  and  $\hat{x}_2$  for which the normal distributions variances  $\sigma_{x_i}$  are independent. They are obtained by simply rotating the coordinate system by  $\theta$ . We compare the actual and fitted distributions in *c)*. We introduce the metric  $d$ , see eq. 5, to measure and minimize the distance of the estimated normal distributions and real distributions. With the set  $X_{S_i}$  containing all grid points  $\vec{x}_i$  that belong to a source  $S_i$ , we want to minimize  $d_{S_i}$  for all assumed sources  $S_i \in S$  in the beamforming map.

$$d_{S_i} = \sum_{\vec{x}_i \in X_{S_i}} \left| \text{hist}(\vec{x}_i) - \sum_{S_i \in S} (\text{PDF}_{S_i}(\vec{x}_i)) \right| \quad (5)$$

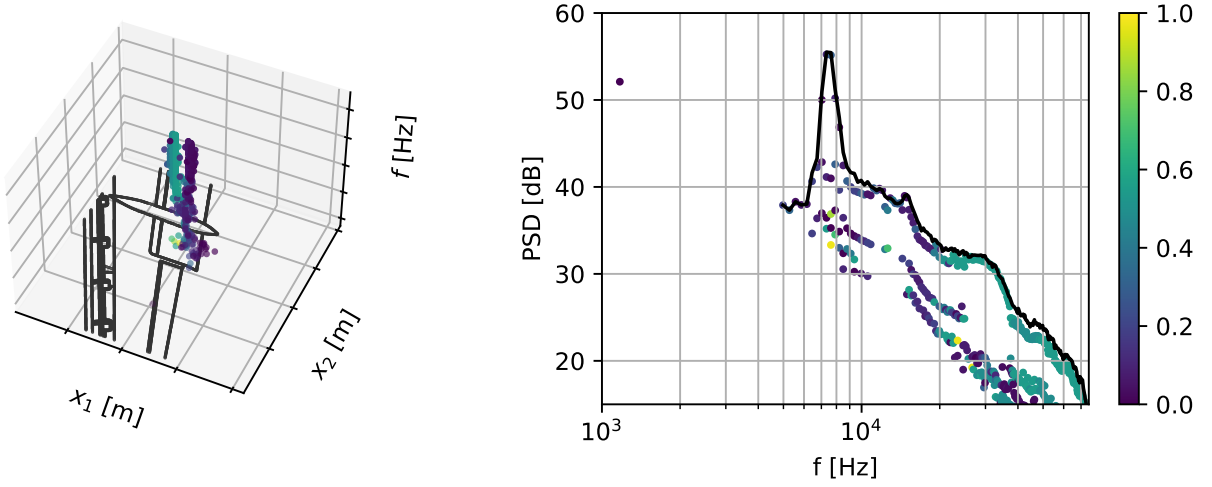


Figure 4: The source-parts at the A320 flap side edge at  $M = 0.175$ ,  $\alpha = 9^\circ$  from the SIND-solution that lie within  $1 - 3\sigma$  confidence. The confidence (normalized PDF-value) that the source-part belongs to the source is displayed in color. The black line represents the integrated spectrum from all source-parts.

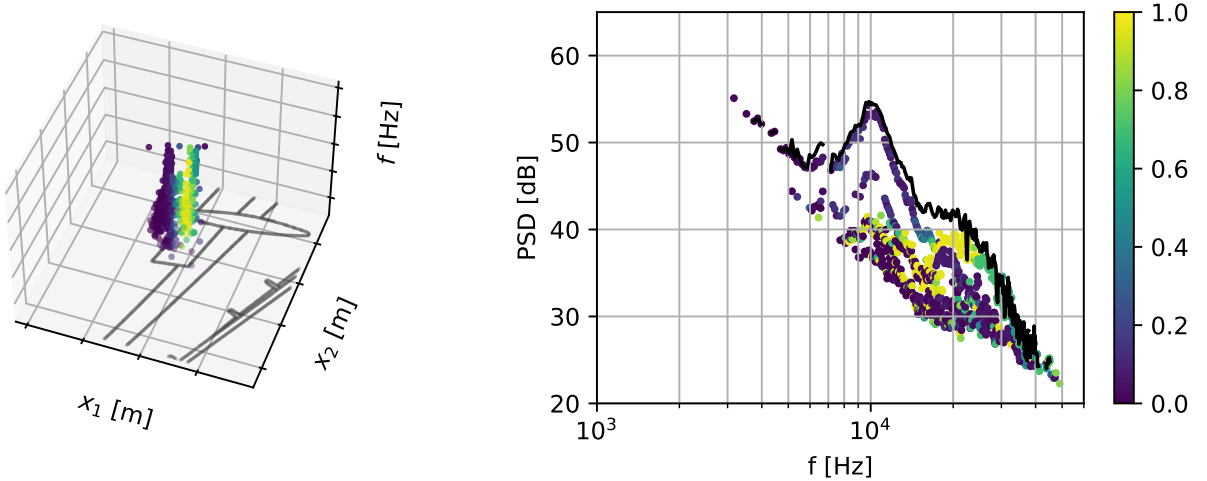


Figure 5: The source-parts at the Do728 flap side edge at  $M = 0.250$ ,  $\alpha = 7^\circ$  from the SIND-solution that lie within  $1 - 3\sigma$  confidence. The confidence (normalized PDF-value) that the source-part belongs to the source is displayed in color. The black line represents the integrated spectrum from all source-parts.

Using this metric we can implement a greedy algorithm that minimizes  $d_{S_i}$  iteratively. First, we find the maximum in the histogram of the source-parts; second, we fit a normal distribution that minimizes the histogram; and third, we subtract the fitted distribution from the histogram and repeat the process until the remaining histogram-maximum drops below a threshold  $t_I$ . This threshold represents a lower significance bound. After subtracting a PDF from the histogram, occasionally single  $\vec{x}_i$  with a high source-part count remains due to fitting inaccuracies (single beamforming map pixel are then fitted with a distribution). We integrate the total PDF area  $A_{S_i} = \int_{x_1} \int_{x_2} \text{PDF}(S_i) dx_2 dx_1$  for each source to account for these artifacts. If  $A_{S_i}$  drops below a threshold  $t_A$  we can reject it as a fitting artifact.  $A_{S_i}$  of artifacts is orders of magnitude

below  $A_{S_i}$  of real sources.

Figure 10 a) shows the result of the procedure for the A320. The threshold  $t_I$  for the iterating process is  $t_I = 20$  source-parts. No sources are rejected as fitting artifacts. The crosses mark the determined sources, the numbers correspond to the order in which they are identified. The ellipses around the marked sources represent  $\text{PDF}_S(\vec{x}) = 1 - 2\sigma$  of the fitted normal distributions. Figure 11 a) shows the result of the procedure for the Do728 for  $t_I = 30$ , no sources are rejected as fitting artifacts.

Finally, we calculate for all found source-parts their probability of belonging to each source-cluster using  $\text{PDF}_S$  and assign them to the source with the highest probability. Then we drop all source-parts with a PDF value below a threshold  $t_\sigma$ . Figure 4 shows the source-parts that were assigned to the flap side edge within  $t_\sigma = 3\sigma$  confidence at  $M = 0.125$ ,  $\alpha = 9^\circ$ . The color encodes the corresponding normalized PDF value, which can be interpreted as the confidence that the source-parts belong to the assigned source. We observe three rows of points with similar shape over frequency. We assume that the two rows at a low SPL are artifacts from the CLEAN-SC process, as CLEAN-SC failed to remove these source-parts from the dirty map without residue. After integrating all source-parts over the frequency, we obtain a mostly smooth spectrum, indicated by the black line. Figure 5 shows the same for the Do728 at  $M = 0.250$ ,  $\alpha = 7^\circ$ .

## B. Source Identification based on Hierarchical Clustering (SIHC)

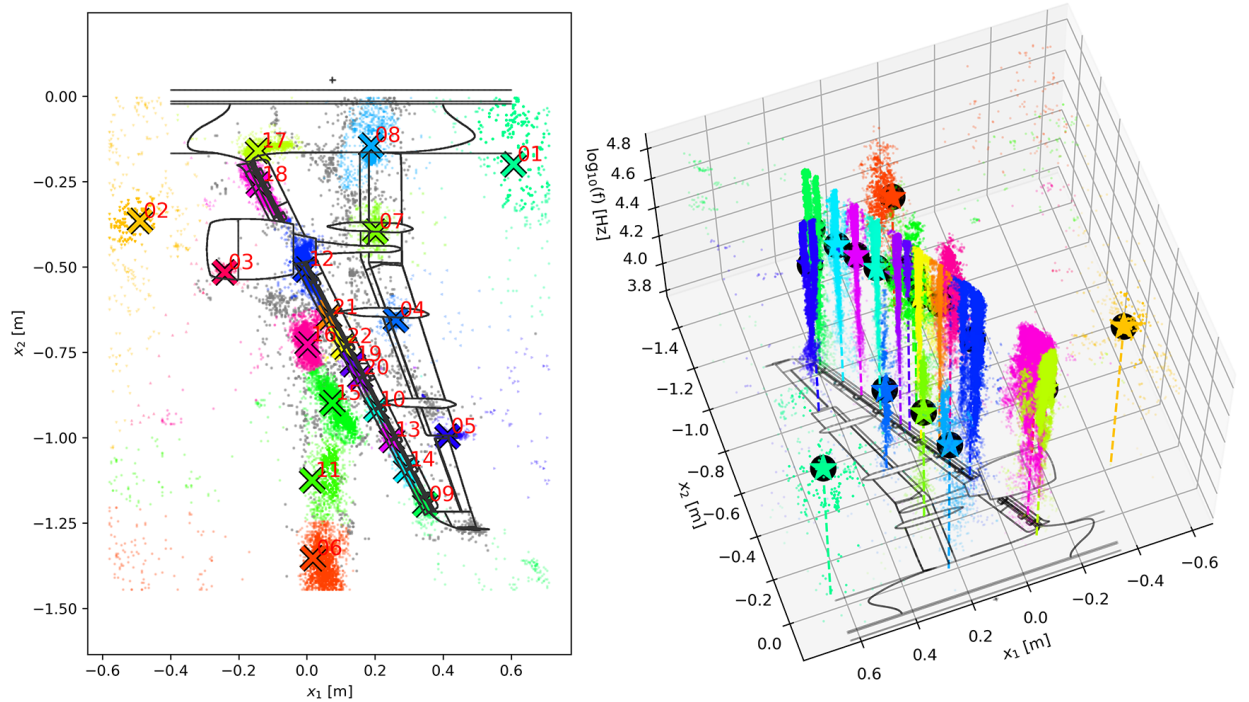


Figure 6: A320. Resulting clusters from HDBSCAN, using an euclidean distance metric. The cluster midpoints are marked with an X or a star, the corresponding source-parts are displayed in the same color. The transparency level displays the probability of belonging to the cluster. Grey source-parts were rejected as noise.

A second approach to identifying sources and assigning the corresponding source-parts is clustering methods which can automatically group points in a multidimensional space. Since we do not know the number of expected clusters and their distribution beforehand, we choose Hierarchical Density-Based Spatial Clustering of Applications with Noise<sup>8</sup> (HDBSCAN). Similar to SIND, HDBSCAN requires a threshold below which a cluster is rejected as noise. We cluster the source-parts based on their normalized location  $\vec{x}_i$ , normalized Strouhal number  $\text{St}_i$  and normalized, scaled PSD level (normalized to the range  $[0, 1]$ ). When clustering source-parts of maps at different Mach numbers at the same time, we recommend using a Mach scaled PSD



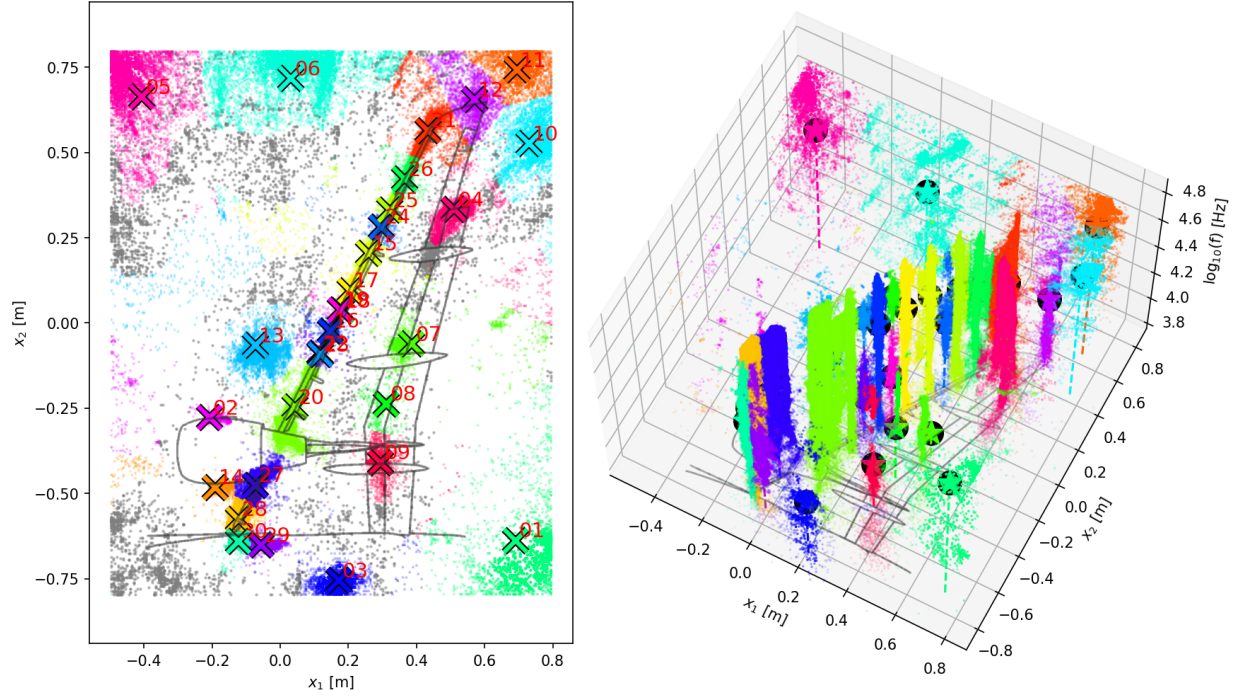


Figure 7: Do728. Resulting clusters from HDBSCAN, using an euclidean distance metric. The cluster midpoints are marked with an X or a star, the corresponding source-parts are displayed in the same color. The transparency level displays the probability of belonging to the cluster. Grey source-parts were rejected as noise.

with  $\widehat{\text{PSD}} = \text{PSD} - 10 \log M^n$  with  $n \approx 5.5$ . This scaling ensures that the source-parts of sources at different Mach numbers are roughly at the same location in the frequency and PSD-level space, as aeroacoustic noise generally scales around this Mach exponent.<sup>5</sup>

Figure 6 shows the result of HDBSCAN for the A320 and Figure 7 for the Do728. The “X” and stars mark the cluster midpoints of the corresponding source-parts, displayed in the same color. Grey source-parts are rejected as noise as their confidence of belonging to any source is below  $t_\sigma = 1 - 3\sigma$ . In the image on the right, a dotted line supports the 3D-localization of the cluster midpoints. The color intensity displays the classification confidence. Figure 8 shows the A320 source-parts that were assigned to the flap side edge at  $M = 0.125$ ,  $\alpha = 9^\circ$  within  $t_\sigma = 1 - 3\sigma$  confidence, Figure 9 shows the same for the Do728.

### C. Comparison of SIND and SIHC

Figure 10 shows the comparison of the identified sources with SIND the SIHC for the A320, Figure 11 shows the same comparison for the Do728. We fit normal distributions to the source-parts that are clustered by SIHC in b) which allows us to compare the resulting source positions and integration areas. These normal distributions are only for visual support, the real source-distributions for SIHC are shown in Figure 6 and Figure 7.

Both methods yield similar overall results and are able to identify the prominent source locations. On the one hand, SIND is able to separate individual sources that are clustered together by SIHC, especially in the slat region. On the other hand, SIHC is able to find source regions that are not well localized and spread over the map, especially sources that are not located on the wing. We observe that SIND and SIHC assume different underlying source distributions when comparing the resulting flap side edge spectra in Figure 4 and Figure 8 for the A320 and Figure 5 and Figure 9 for the Do728. However, the resulting integrated spectra are nearly identical for the A320 and similar for the Do728. Performance-wise SIHC’s computation time scales around  $\mathcal{O}(n \log n)$  for the number  $n$  of source-parts.<sup>8</sup> Since SIND does not cluster the points directly, the

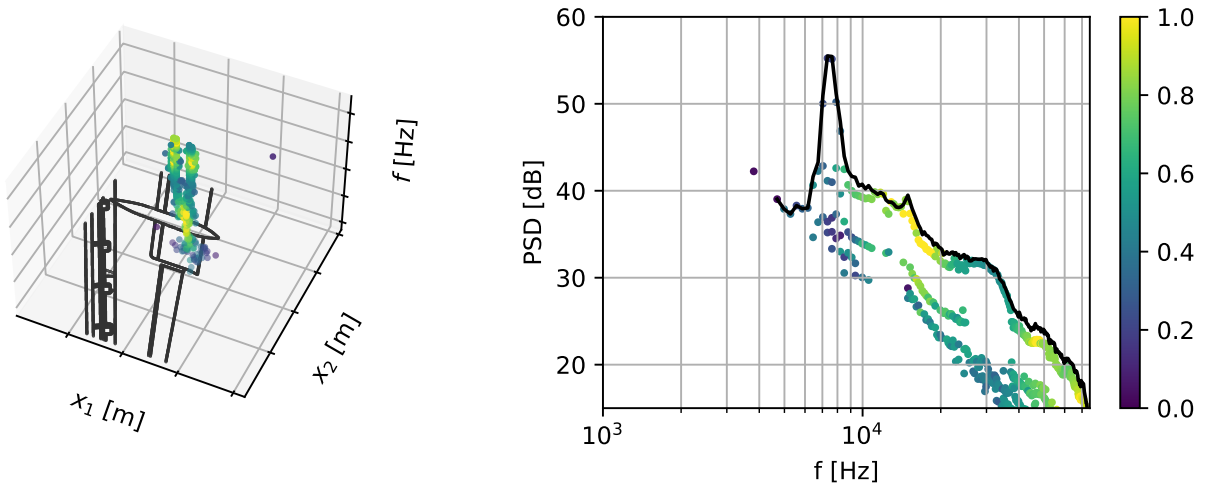


Figure 8: The source-parts at the A320 flap side edge at  $M = 0.175$ ,  $\alpha = 9^\circ$  from the SIHC-solution that lie within  $1 - 3\sigma$  confidence. The confidence (normalized PDF-value) that the source-part belongs to the source is displayed in color. The black line represents the integrated spectrum from all source-parts.

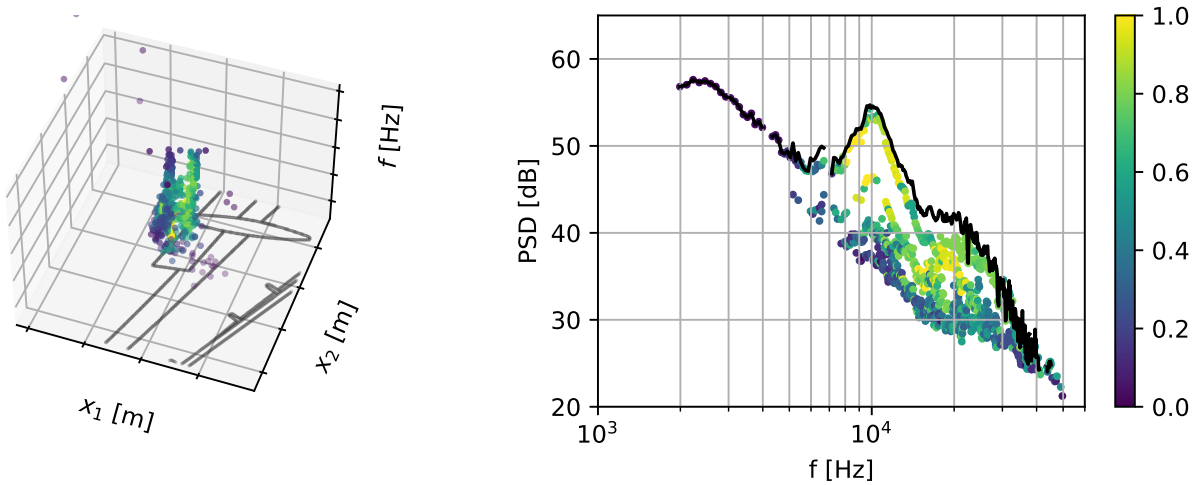


Figure 9: The source-parts at the Do728 flap side edge at  $M = 0.125$ ,  $\alpha = 7^\circ$  from the SIHC-solution that lie within  $1 - 3\sigma$  confidence. The confidence (normalized PDF-value) that the source-part belongs to the source is displayed in color. The black line represents the integrated spectrum from all source-parts.



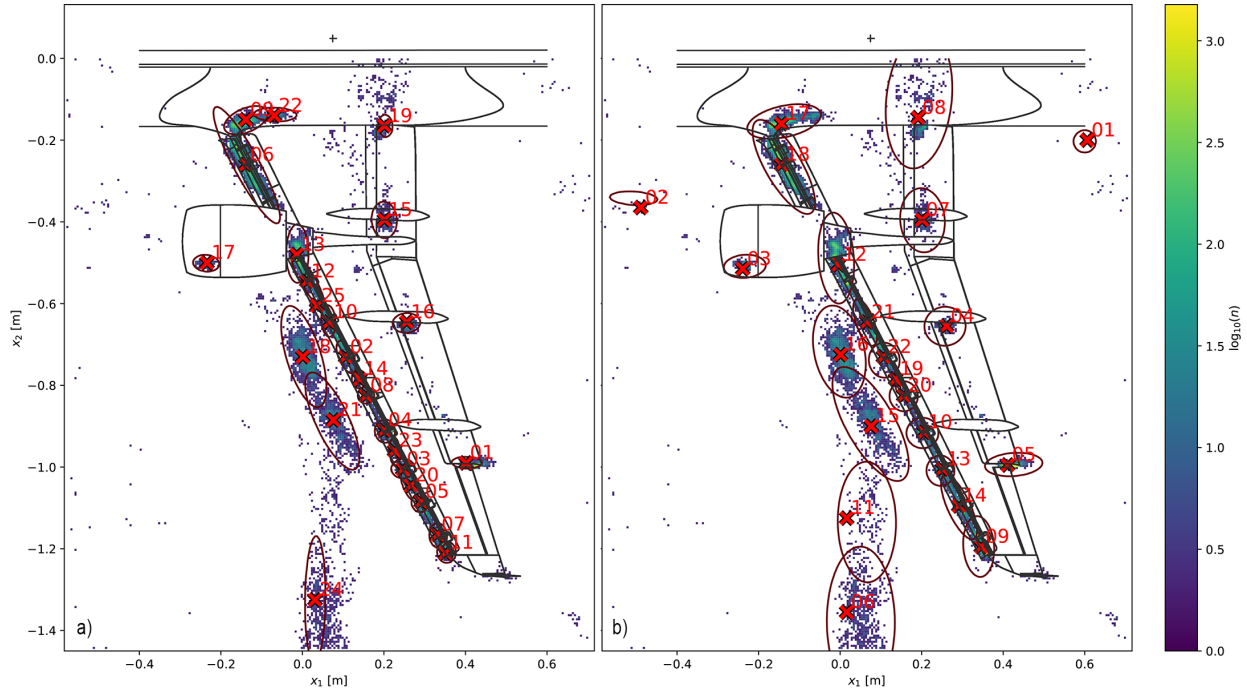


Figure 10: A320. *a)* shows the SIND solution for all sources above  $t_i = 20$  within  $t_\sigma = 1 - 3\sigma$ . The source numbers correspond to the order of found sources via the maxima in the histogram. *b)* shows normal distributions that are fitted to the source-parts that were clustered by SIHC. The ellipses around the sources represent the PDF functions at  $1 - 2\sigma$ . The colored points are the log-histogram values from all source-parts.

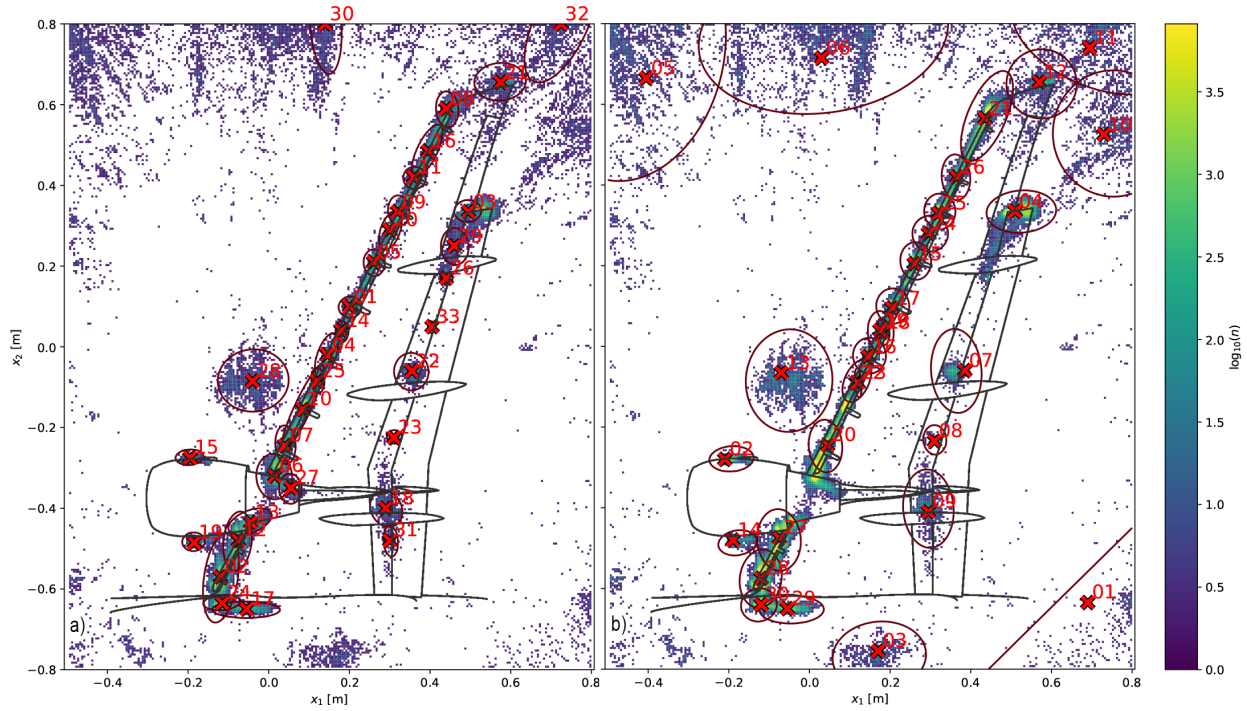


Figure 11: Do728. *a)* shows SIND solution for all sources above  $t_i = 30$  within  $t_\sigma = 1 - 3\sigma$ . The source numbers correspond to the order of found sources via the maxima in the histogram. *b)* shows normal distributions that are fitted to the source-parts that were clustered by SIHC. The ellipses around the sources represent the PDF functions at  $1 - 2\sigma$ . The colored points are the log-histogram values from all source-parts.

computation time is independent of the number of points, which is a huge advantage for large datasets. The total number of source-parts in the Do728 dataset is around  $n = 10^6$ , which SIND processes within seconds and SIHC within an hour on a normal laptop. Both methods process the A320 dataset within seconds, which contains around  $n = 10^4$  source-parts.

## IV. Discussion

We presented two methods on how to detect sources and extract their PSD from CLEAN-SC-deconvolved beamforming maps. SIND was based on the idea that the source-parts of real acoustic sources appear spatially normal distributed in CLEAN-SC maps. Thus, it yielded good results in finding point-like sources such as the slat tracks and the strake in both datasets. The identification of line-like sources, such as the slat, is difficult for this approach. The resulting low frequency slat tones<sup>4</sup> are visible in Figure 1 between the slat tracks. SIND identified these as multiple point-like sources due to its distribution assumption in combination with CLEAN-SC processing, while SIHC often included these in the slat-track sources, see Figure 6. SIND was also able to identify overlapping sources or point-like sources that were embedded in distributed sources such as the nacelle region. Its results were consistent with the expert out of the loop since the introduced thresholds don't affect the source identification. SIHC was based on hierarchical clustering methods and thus did not assume a predefined source distribution. The source-parts were clustered directly in space, frequency, and SPL with the expert in the loop, as the results depend strongly on the set threshold. Both methods identified the prominent source locations correctly.

Most of the determined source-part clusters were similar, but there were differences in the way both methods handled source-part blobs of different densities. While SIND handled very dense source-part blobs with a clear midpoint well and profited from stacking the histograms of multiple measurements at different Mach numbers and angles of attack, it failed to recognize sparse source blobs with no clear midpoint. Wind-tunnel noise was a prominent example for this, as this source was projected on different parts of the image with increasing angle of attack  $\alpha$ . SIHC handled loose source distributions such as the wind-tunnel noise well, but tended to cluster high density source blobs together that SIND separated into multiple sources. For the A320, both SIND and SIHC predicted the inner slat to be a single source, while we assume from Figure 1 that there are at least two slat tracks, embedded in a distributed high frequency noise source. For the Do728, both methods identified the two slat tracks at the inner slat. SIND additionally identified the gap between the nacelle and inner slat. SIND also identified additional sources in the flap region.

Despite the similar source position identifications, the resulting spectra featured prominent differences in the low-frequency region, see Figure 9 and Figure 5. While the well-localized high-frequency source-parts dominated SIND's normal distributions, SIHC identified source-distributions that featured multiple regions of high confidence in space, frequency, and SPL. We observed this behavior on the flap side edge, the significance of SIND's distribution decreased towards low frequencies as the source-parts move further downstream. This effect resulted from the limitations of CLEAN-SC in combination with assuming a normal distribution as we expect the flap side edge to be a line-source with a frequency-dependent source location.<sup>6</sup> SIHC performed better in identifying the underlying source distribution and in finding the corresponding low-frequency source-parts. It had the advantage, that the clustering considered the frequency and SPL information which enabled it to identify the corresponding low-frequency source-parts, that were scattered spatially around the whole map. This is important, as low-frequency noise generally carries most of the acoustic energy. Both methods identified the same spectrum for the A320 flap side edge. For the Do728, SIND reconstructed the spectrum down to  $f = 3$  kHz, while SIHC reconstructed the spectrum down to  $f = 2$  kHz. Since SIHC also included parts of the top Do728 flap track into the flap side edge, it is unclear which result is correct in this case. Regarding the slat, SIND's separation of slat track and slat was correct but suffered from the low array resolution, so the low-frequency slat tones were often assigned incorrectly to neighboring source positions. Since SIHC often clustered slat and slat track together, it yielded much more consistent spectra at the cost of less spatially distinguished sources.

Both methods proved useful with different advantages and disadvantages to the real-world airframe datasets. SIHC works well for small datasets (e.g., a single angle of attack and few Mach variations) with little statistical noise. It is a great tool to explore the dataset because a single-threshold drastically changes

the outcome. Generally, density-based clustering methods tend to fail separate clusters when too much noise is present that connects the clusters, so-called bridge points. Consequently, HDBSCAN yields better results when decreasing the Welch block size, which increases the number of FFT averages and results in less statistical noise but also a lower frequency resolution. SIND works well for noisy datasets with high-resolution PSDs (large Welch block sizes) and yields stable results, that are mostly independent of the selected thresholds and profits from large datasets. While the  $t_I$  threshold limits the processing time and prevents endless loops, the  $t_A$  threshold only drops clusters after the identification. Increasing or decreasing these values will not change the outcome of the remaining sources. Thus, SIHC is well-suited for an iterative process with the expert in the loop, while SIND requires less tuning to generate stable results and can be employed autonomously. In specific cases, when two sources overlap spatially but can be distinguished based on their  $\text{PSD}(f)$ , the SIHC method has a clear advantage. While dense source-distributions with bridge-points are problematic for SIHC, it was able to detect sparse source-distributions without a clear midpoint, which SIND cannot detect. Performance-wise SIND is superior to SIHC and can be employed on datasets of any size. Together, both methods cover the automatic source identification and spectrum generation from single, sparse low-resolution FFT beamforming maps to high-resolution FFT beamforming maps including multiple parameter variations with speed and accuracy that is unmatched by human experts.

## V. Conclusion

We presented the two methods “SIND” and “SIHC”, which automatically detect aeroacoustic sources in deconvolved beamforming maps. They identify the underlying source-distribution and thus allow for the automatic determination of Regions Of Interest. To the best of our knowledge, these are the first completely automated approaches that can identify sources and generate corresponding spectra from beamforming maps. Both methods together cover a variety of real-world scenario used-cases, from single measurements with sparse source distributions to high-dimensional datasets with parameter variations.

## References

- <sup>1</sup>AHLEFELDT, T. Aeroacoustic measurements of a scaled half-model at high reynolds numbers. *AIAA Journal* 51, 12 (2013), 2783–2791.
- <sup>2</sup>AHLEFELDT, T. Microphone-array measurements on a scaled model at real-flight reynolds numbers. *Journal of Sound and Vibration* 340, 3 (Jan. 2015).
- <sup>3</sup>BAHR, C. J., HUMPHREYS, W. M., ERNST, D., AHLEFELDT, T., SPEHR, C., PEREIRA, A., LECLÈRE, Q., PICARD, C., PORTEOUS, R., MOREAU, D., FISCHER, J. R., AND DOOLAN, C. J. A comparison of microphone phased array methods applied to the study of airframe noise in wind tunnel testing. In *23rd AIAA/CEAS Aeroacoustics Conference* (2017).
- <sup>4</sup>DOBRYNSKI, W., AND POTT-POLLENSKE, M. Slat noise source studies for farfield noise prediction. In *7th AIAA/CEAS Aeroacoustics Conference and Exhibit* (05 2001), vol. 5805.
- <sup>5</sup>GUO, Y. P., AND JOSHI, M. C. Noise characteristics of aircraft high lift systems. *AIAA Journal* 41, 7 (2003), 1247–1256.
- <sup>6</sup>HOWE, M. On the generation of side-edge flap noise. *Journal of Sound and Vibration* 80, 4 (1982), 555 – 573.
- <sup>7</sup>HOWE, M. S. *Hydrodynamics and Sound*. Cambridge University Press, 2007.
- <sup>8</sup>MCINNES, L., HEALY, J., AND ASTELS, S. hdbscan: Hierarchical density based clustering. *The Journal of Open Source Software* 2, 11 (mar 2017).
- <sup>9</sup>MERINO-MARTINEZ, R., SIJTSMA, P., RUBIO CARPIO, A., ZAMPONI, R., LUESUTTHIVIBOON, S., MALGOEZAR, A., SNELLEN, M., SCHRAM, C., AND SIMONS, D. Integration methods for distributed sound sources. *International Journal of Aeroacoustics* 18 (06 2019), 1475472X1985294.
- <sup>10</sup>MERINO-MARTÍNEZ, R., SIJTSMA, P., SNELLEN, M., AHLEFELDT, T., ANTONI, J., BAHR, C. J., BLACODON, D., ERNST, D., FINEZ, A., FUNKE, S., GEYER, T. F., HAXTER, S., HEROLD, G., HUANG, X., HUMPHREYS, W. M., LECLÈRE, Q., MALGOEZAR, A., MICHEL, U., PADOIS, T., PEREIRA, A., PICARD, C., SARRADJ, E., SILLER, H., SIMONS, D. G., AND SPEHR, C. A review of acoustic imaging methods using phased microphone arrays. *CEAS Aeronautical Journal* 10, 1 (Mar 2019), 197–230.
- <sup>11</sup>MÜLLER, E.-A., Ed. *Mechanics of Sound Generation in Flows*. IUTAM Symposia. Springer-Verlag Berlin Heidelberg, Aug. 1979.
- <sup>12</sup>SIJTSMA, P. Experimental techniques for identification and characterisation of noise sources. Tech. rep., NLR, 2004.
- <sup>13</sup>SIJTSMA, P. Clean based on spatial source coherence. international journal of aeroacoustics. *International Journal of Aeroacoustics* 6 (2007).